AIMS Mathematics, 11(11): 38242–38270.
DOI:10.3934/math.20261477
Received: 05 September 2026
Revised: 19 October 2026
Accepted: 26 October 2026
Published: 17 November 2026

https://www.aimspress.com/journal/Math

Research article

Compact implicit high-resolution numerical scheme for multicomponent transport problems with Langmuir sorption

Dagmar Žáková* **and Peter Frolkovič**

Department of Mathematics and Descriptive Geometry, Faculty of Civil Engineering, Slovak University of Technology in Bratislava, Bratislava, Slovakia

* **Correspondence:** Email: dagmar.zakova@stuba.sk.

Abstract: We present a compact implicit high-resolution finite volume scheme for one-dimensional multicomponent transport problems with nonlinear Langmuir sorption. The method combines a second-order compact implicit discretization with Weighted Essentially Non-Oscillatory (WENO) reconstruction and a time limiter for the treatment of steep gradients and discontinuities. Special attention is given to the Courant number used in the limiter, where local characteristic Courant numbers based on the eigenvalues of the inverse retardation matrix were considered. The compact implicit schemes were compared with analogous explicit first-order and second-order methods. Numerical experiments showed second-order convergence for smooth solutions and demonstrated that the implicit approach can be used with significantly larger Courant numbers. The method was also applied to a three-component displacement chromatography problem with sharp concentration fronts.

Keywords: compact implicit scheme; high-resolution method; WENO reconstruction; finite volume method; multicomponent transport; Langmuir sorption; nonlinear chromatography
Mathematics Subject Classification: 35L60, 35L65, 65M08, 65M12

1. Introduction

For many years, there has been a growing interest in mathematical models describing the transport of substances in porous media, where the migration of solute components is significantly influenced by their interaction with the solid matrix through sorption or adsorption processes. This class of problems plays a key role in at least two important applications: the simulation of contaminant transport in groundwater systems [1–3] and the modeling of preparative liquid chromatography [4–6]. Additional numerical studies address contaminant transport in groundwater [7], transport with sorption isotherms [8], and reactive liquid chromatography [9].

In this paper, we focus our attention purely on the underlying mathematical model, clearly motivated

by these two important engineering applications. Moreover, we concentrate only on the advective part of the transport and skip the treatment of diffusion-dispersion processes, referring to standard approaches to include them [7,10]. Consequently, in our study, we are dealing formally with hyperbolic partial differential equations [11, 12] given by first-order hyperbolic systems [13].

For such transient problems governed by partial differential equations, to be solved numerically, two fundamental classes of time discretization can be considered. The first and often preferred approach is represented by explicit methods, which deliver numerical solutions directly without the need to solve algebraic systems of equations. However, explicit schemes are constrained by stability restrictions on the choice of the time step, such as the Courant–Friedrichs–Lewy (CFL) condition [11]. Conversely, the second approach consists of implicit methods. Although, in general, they lead to the necessity of solving systems of algebraic equations at each time level, they offer unconditional stability, allowing the time step to be selected based solely on accuracy requirements rather than stability constraints [11, 14].

The situation becomes significantly different when the mathematical model contains a system of differential equations with nonlinearity under the time derivative, as occurs in the presence of nonlinear accumulation terms due to, e.g., sorption isotherms. In this case, the problem to be solved is described by a system of strongly coupled transport-reaction equations, where even explicit methods are forced to solve local, nonlinear algebraic equations at each grid cell to recover physical concentrations from the conserved variables under the time derivative. Furthermore, any standard explicit discretization of each individual differential equation in a component-wise manner fails to respect the strong coupling with the remaining equations in the system.

For this class of problems, implicit methods of time discretization appear to be highly advantageous, provided that they can bypass the computationally expensive task of solving large, globally coupled, nonlinear algebraic systems. To address this challenge, we present a compact implicit numerical method [8, 14, 15], which, similar to explicit approaches, requires only the resolution of small, local systems of algebraic equations in each grid cell while fully respecting the tight coupling of the transport-reaction equations in the system.

In this paper, we develop a high-resolution, compact implicit numerical scheme that is tailored to solve transport equations coupled through fast sorption processes using popular Langmuir isotherms [7, 10, 12, 13]. For smooth solutions, the method is second-order accurate, and it can compete very well with analogous explicit numerical methods, as it is not restricted by the CFL condition for the choice of time steps. This is a very important advantage in cases where some of the solutes (which may not be of large interest for a particular application) are transported quickly with respect to others. If, for instance, such solutes leave the computational domain, the implicit method can enlarge the time step, which accurately approximates the slow components. This is not possible for explicit schemes, where the choice of time step must still respect the fastest transport even if the corresponding transported component is not present in the domain. An illustrative numerical example is given later in this paper.

As the governing partial differential equations belong formally to the class of nonlinear hyperbolic systems, it is well-known that the solution of such problems can develop discontinuities (shocks) even for initially smooth profiles. Moreover, numerical methods in the presence of such nonsmooth solutions will develop unphysical oscillations that can completely destroy the plausibility of numerical results. Therefore, we extend the second-order accurate form of the scheme to the high-resolution form that can locally adjust the stencil of the numerical scheme analogously to (weighted) essentially

non-oscillatory-type approximations [13, 14, 16] or limit the approximation locally toward a first-order accurate scheme that is necessary only in some situations when time steps violate the CFL condition [14, 15, 17, 18].

In summary, the novelty of the presented numerical method is a compact implicit time discretization of the advection term in the system of transport equations coupled through sorption isotherms that is not significantly more computationally demanding than comparable explicit discretizations. The main motivation is to offer a numerical method that is unconditionally stable, so there is, opposite to previous treatments using explicit discretization of advection [5, 9, 10], no impractical stability restriction on the choice of time steps if uninteresting components with fast advective transport occur in the model. Such a class of numerical methods has recently gained popularity for standard hyperbolic systems [15, 18, 19], but, to our knowledge, they are not available for hyperbolic systems given as coupled transport equations. Such systems, in general, cannot be transformed to the standard form of hyperbolic conservation laws, so the presented work is the first attempt to fill this unresolved research gap. We demonstrate with several numerical experiments that the situations in which explicit numerical schemes are impractical due to stability restrictions on time steps that are much higher than required by accuracy requirements can occur for this kind of problem.

The paper is organized as follows: Section 2 introduces the mathematical model, first for a scalar transport equation with Langmuir sorption and then for the corresponding multicomponent system. Section 3 presents the first-order and second-order compact implicit schemes together with the analogous explicit discretizations. The high-resolution formulation, including the WENO reconstruction, time limiter, and characteristic Courant numbers, is described in Section 4. Numerical experiments are presented in Section 5, including a smooth three-component Langmuir problem, a linear benchmark problem, and a three-component displacement chromatography example. Finally, conclusions are presented in the last section.

2. Mathematical model

2.1. Scalar transport equation with sorption

To introduce the topic more clearly, we first consider a representative nonlinear scalar transport problem in a porous medium [1,2,7,12]. Let $c = c(x,t) \geq 0$ denote the concentration of the transported substance, where $t \in (0,T)$ and $x \in (x_L, x_R) \subset R$. The transport of the mobile phase is driven by a given constant velocity $u > 0$. The governing equation is written in the conservative form

$$F(c)_t + (uc)_x = 0\,, \tag{2.1}$$

with the prescribed initial condition

$$c(x,0) = c^0(x)\,. \tag{2.2}$$

While $c = c(x,t) \geq 0$ denotes the mobile concentration, $F(c)$ describes the total concentration, including both the mobile and adsorbed phases, as given by

$$F(c) = c + \frac{1-\varepsilon}{\varepsilon}\Psi(c)\,, \tag{2.3}$$

where $\varepsilon \in (0,1)$ denotes the porosity of the medium, i.e., the ratio of the void space that can be filled by the liquid solution to the total volume of the porous medium, and $\Psi(c)$ denotes the sorption isotherm.

The factor

$$R = \frac{1-\varepsilon}{\varepsilon} \tag{2.4}$$

measures the relative contribution of the adsorbed phase to the mobile phase.

The mathematical model can describe not only the transport of contaminants [1, 2, 12] but also transport processes in chromatography [4, 20, 21] with sorption isotherms. Further numerical approaches to chromatographic transport are presented in [5, 10, 13]. In this work, we consider the nonlinear Langmuir sorption isotherm [5, 10, 13], which is widely used in models of sorption and chromatography [1, 20, 21], defined as

$$\Psi(c) = \frac{ac}{1+bc}, \qquad a, b > 0, \tag{2.5}$$

where a characterizes the amount of adsorbed substance and b controls how rapidly the adsorption approaches its saturation value. Consequently, $F(c)$ is

$$F(c) = c + \frac{1-\varepsilon}{\varepsilon}\frac{ac}{1+bc}, \tag{2.6}$$

with the derivative of the function

$$F'(c) = 1 + \frac{1-\varepsilon}{\varepsilon}\frac{a}{(1+bc)^2}. \tag{2.7}$$

Since $a, b > 0$ and $0 < \varepsilon < 1$, we have

$$F'(c) > 1 \qquad \text{for all } c \geq 0. \tag{2.8}$$

The Eq (2.1) can also be written in the form (if all involved derivatives exist)

$$F'(c)c_t + uc_x = 0. \tag{2.9}$$

Equivalently, in the primitive variables formulation, or the nonconservative formulation [11, 12], it is

$$c_t + \frac{u}{F'(c)}c_x = 0, \tag{2.10}$$

where

$$\lambda(c) = \frac{1}{F'(c)}, \tag{2.11}$$

so that $u\lambda(c)$ is the nonlinear characteristic speed.

Since $u > 0$ and $F'(c) > 1$ for $c \geq 0$, the characteristic speed is positive. Therefore, a Dirichlet boundary condition is prescribed only at the inflow boundary $x = x_L$ [11],

$$c(x_L, t) = c_{x_L}(t), \tag{2.12}$$

while no boundary condition is required at the outflow boundary $x = x_R$.

The sorption term introduces nonlinear retardation into the transport process. Larger values of $F'(c)$ correspond to stronger retardation and therefore to smaller characteristic speeds. In particular, increasing the adsorption parameter a or decreasing the porosity ε increases the retardation effect. On the other hand, if the sorption is weak, then $F'(c)$ is close to one and the characteristic speed is close to the transport velocity u.

2.2. Extension to a system of equations

We now extend the scalar model to a system of transported concentrations. Let N_c denote the number of transported components. We introduce the vector

$$C = (c_1, c_2, \ldots, c_{N_c}) \tag{2.13}$$

of mobile concentrations, where $c_m = c_m(x,t) \geq 0$, $m = 1, \ldots, N_c$. The transport of all components is driven by the same constant velocity $u > 0$. With

$$F(C) = \left(F_1(C), F_2(C), \ldots, F_{N_c}(C)\right), \tag{2.14}$$

where $F_m = F_m(C)$ denotes the total concentration of the m-th component, $m = 1, \ldots, N_c$, the governing system is written in the form

$$F_m(C)_t + (uc_m)_x = 0, \qquad m = 1, \ldots, N_c, \tag{2.15}$$

or, equivalently, in the vector form,

$$F(C)_t + (uC)_x = 0. \tag{2.16}$$

The initial condition is prescribed by

$$C(x,0) = C^0(x), \tag{2.17}$$

or equivalently,

$$c_m(x,0) = c_m^0(x), \qquad m = 1, \ldots, N_c. \tag{2.18}$$

For the system, we again consider a Langmuir sorption isotherm, with $F_m(C)$ defined as

$$F_m(C) = c_m + \frac{1-\varepsilon}{\varepsilon} \frac{a_m c_m}{1 + \sum_{j=1}^{N_c} b_j c_j}, \qquad m = 1, \ldots, N_c. \tag{2.19}$$

This multicomponent form of the Langmuir isotherm is commonly used in mathematical models of nonlinear chromatography [10, 20, 22].

To derive the quasilinear form of the system, we apply the chain rule. Let

$$J(C) = \frac{\partial F}{\partial C} \tag{2.20}$$

be the Jacobian matrix of the mapping $F(C)$, with entries

$$J_{mj}(C) = \frac{\partial F_m}{\partial c_j}(C), \qquad m, j = 1, \ldots, N_c. \tag{2.21}$$

Then

$$F(C)_t = J(C)C_t. \tag{2.22}$$

Therefore, system (2.16) can be written as

$$J(C)C_t + uC_x = 0. \tag{2.23}$$

If $J(C)$ is invertible, this is equivalent to

$$C_t + uJ(C)^{-1}C_x = 0\,. \tag{2.24}$$

The matrix $J(C)$ plays the role of a nonlinear retardation matrix. If $\mu_m(C)$, $m = 1, \ldots, N_c$, are the eigenvalues of $J(C)$ and

$$\lambda_m(C) = \frac{1}{\mu_m(C)}, \qquad m = 1, \ldots, N_c\,, \tag{2.25}$$

are eigenvalues of $J(C)^{-1}$, then the characteristic speeds of the system are given by the eigenvalues $\lambda_m(C)$ [5, 13, 23] multiplied by the transport velocity u.

Thus, large eigenvalues of $J(C)$ correspond to strong retardation and slow wave propagation, while eigenvalues close to one correspond to weak retardation and faster transport [5, 13].

In the Langmuir case considered here, the eigenvalues of $J(C)$, and also $J(C)^{-1}$, are positive [5, 10, 13, 24], and therefore the direction of propagation is determined by the sign of the transport velocity u. In all numerical experiments presented here, we assume $u > 0$, so that all characteristic waves propagate from left to right.

Since the velocity and eigenvalues are all positive, boundary conditions are prescribed only at the inflow boundary $x = x_L$,

$$C(x_L, t) = C_{x_L}(t)\,, \tag{2.26}$$

while no boundary condition is imposed at the outflow boundary $x = x_R$.

3. Second-order accurate schemes

In this section, we briefly describe the numerical schemes used in the computations. Our aim is to highlight the advantages of several variants of the compact implicit scheme when applied to this kind of problem. The detailed derivation of the compact implicit high-resolution method was presented in [8, 15]. Here, we recall only the main information and adapt the process to the multicomponent Langmuir system considered in this paper.

The spatial discretization is based on the finite volume method [11, 25]. The computational domain is divided into finite volumes $I_i = (x_{i-1/2}, x_{i+1/2})$, $i = 1, \ldots, M$, with uniform mesh size h. The time levels are denoted by $t^n = n\tau$, where τ is the time step and $n = 0, \ldots, N$. For system (2.15), we denote by C_i^n the numerical approximation of the vector of concentrations associated with the finite volume I_i at time t^n. The corresponding accumulated concentration is denoted by $Q_i^n = F(C_i^n)$.

A finite volume discretization of the governing system over I_i and the time interval (t^n, t^{n+1}) leads to

$$Q_i^{n+1} - Q_i^n + \frac{\tau}{h} u \left(C_{i+1/2}^{n+1/2} - C_{i-1/2}^{n+1/2} \right) = 0\,, \tag{3.1}$$

where $C_{i+1/2}^{n+1/2}$ denotes a suitable approximation of the time-averaged concentration at the cell interface. Since, in this work, we assume $u > 0$, all numerical fluxes are evaluated using left-biased upwind stencils [11, 25]. For cases in which $u < 0$, see [8].

3.1. Compact implicit scheme

For comparison purposes, we use the first-order implicit upwind scheme. In this case, the interface value is approximated simply by $C_{i+1/2}^{n+1/2} = C_i^{n+1}$. The resulting scheme is robust but introduces significant numerical diffusion, especially near sharp concentration fronts [11, 25], see the numerical experiments that come later.

The second-order compact implicit scheme is obtained by replacing the interface value with a compact second-order approximation involving values from the new and previous time levels [8,14,15]. In the scalar case, the detailed derivation follows from a Taylor expansion in space and time. In the present system case, the same construction is applied componentwise to the vector C:

$$C_{i+1/2}^{n+1/2} = C_i^{n+1} - \frac{1}{2}(\omega(C_{i-1}^{n+1} - C_i^n) + (1-\omega)(C_i^{n+1} - C_{i+1}^n)), \tag{3.2}$$

with $\omega \in [0, 1]$.

It is important to note that the resulting compact implicit scheme given by (3.1) with (3.2) contains only unknowns C_i^{n+1}, C_{i-1}^{n+1}, and C_{i-2}^{n+1} that we use to apply efficient algebraic solvers, see later in this section.

For nonsmooth solutions, the second-order approximation may produce oscillations near discontinuities [11, 16, 17]. Therefore, we also use a high-resolution version of the method [8, 14, 15], in which ω changes for each concentration and finite volume I_i, combined with a time limiter, and the scheme then transforms to the form

$$C_{i+1/2}^{n+1/2} = C_i^{n+1} - \frac{1}{2} l_i \circ \left[\omega_i \circ \left(C_{i-1}^{n+1} - C_i^n\right) + (1-\omega_i) \circ \left(C_i^{n+1} - C_{i+1}^n\right)\right]. \tag{3.3}$$

Here, both $\omega_i = (\omega_{1,i}, \ldots, \omega_{N_c,i})$ and $l_i = (l_{1,i}, \ldots, l_{N_c,i})$ are vectors whose components are defined separately for each concentration in the finite volume I_i. The symbol $\circ$ denotes the Hadamard product, and all operations involving ω_i and l_i are understood componentwise, in particular, $1 - \omega_i$ denotes the vector with components $1 - \omega_{m,i}$. Parameter vector ω_i is then computed using a WENO reconstruction [16, 26, 27], see Section 4.1.

In this formulation, both, the WENO approximation and the time limiter l [28] are considered as parts of the numerical scheme, but they play different roles. The WENO approximation is used to determine the reconstruction parameter ω by assigning larger weights to locally smooth stencils and smaller weights to stencils that cross steep gradients or discontinuities. Thus, WENO does not reduce the scheme directly to the first-order approximation; instead, it adapts the reconstruction toward a smoother local stencil. The time limiter l, on the other hand, controls the size of the entire second-order correction. For small Courant numbers or in smooth regions, the time limiter is inactive and should satisfy $l \approx 1$, so that the full second-order approximation is retained. For sufficiently large Courant numbers, particularly near steep fronts or discontinuities, the limiter may decrease toward zero and the scheme is locally reduced toward the first-order upwind method [14, 15, 17].

The obtained system of nonlinear algebraic equations is solved iteratively using the fast sweeping method [19], where each iteration is given by a nonlinear Gauss–Seidel iteration [14, 15, 29]. At each sweep, a local nonlinear algebraic system is solved for every finite volume by Newton's method. Since we consider only positive transport velocities and nonnegative concentrations in the Langmuir transport problems, all characteristic speeds are positive. Consequently, the nonlinear Gauss–Seidel/fast-sweeping method reduces to a single left-to-right sweep through the computational domain at each

time step, from the inflow boundary to the outflow boundary. Therefore, no stopping criterion or tolerance is required for the global iteration. This approach is discussed in more detail in our previous works [8, 14].

The local nonlinear algebraic systems are solved using Newton's method, as mentioned above. The numerical solution from the previous time step is used as the initial guess for each finite volume. We use a maximum of 15 Newton iterations. The iteration is stopped when the norm of the difference between two successive iterates is smaller than 10^{-6}.

Although the compact implicit scheme allows computations with large time steps, the convergence of the local nonlinear solver and the choice of the time limiter remain important for the numerical behavior of the method.

3.2. Explicit schemes

For comparison with the compact implicit schemes, we also implement analogous explicit first-order and second-order accurate schemes. The main motivation for including these methods is to demonstrate that, for the present class of problems, the use of an explicit time discretization is not necessarily computationally advantageous.

The corresponding finite volume update can be written in the form, for $Q_i^{n+1} = F(C_i^{n+1})$,

$$Q_i^{n+1} = Q_i^n - \frac{\tau}{h} u \left(C_{i+1/2}^{n+1/2} - C_{i-1/2}^{n+1/2} \right) , \tag{3.4}$$

where the interface values $C_{i+1/2}^{n+1/2}$ and $C_{i-1/2}^{n+1/2}$ are reconstructed explicitly from the previous time level.

Since the velocity is assumed to be positive, $u > 0$, the first-order explicit scheme is written in the upwind form

$$Q_i^{n+1} = Q_i^n - \frac{\tau}{h} u \left(C_i^n - C_{i-1}^n \right) . \tag{3.5}$$

The right-hand side is known from the previous time level. However, after the update of Q_i^{n+1}, the new concentration vector C_i^{n+1} must still be recovered from the nonlinear relation $F(C_i^{n+1}) = Q_i^{n+1}$, which is solved locally by Newton's method in each finite volume. Note that such a numerical approach is necessary, as an inverse function F^{-1} is not available in general.

The second-order explicit scheme combines a finite volume spatial discretization with a Lax–Wendroff-type time discretization. The latter is based on the Lax–Wendroff-type approach proposed by Qiu and Shu [30]. Their original approach is formulated for hyperbolic systems in the standard conservative form. In the present work, we adopt the Lax–Wendroff-type time discretization idea for system (2.16), where the nonlinear function $F(C)$ appears under the time derivative. Consequently, the replacement of time derivatives by spatial derivatives involves the Jacobian $J(C) = \partial F(C)/\partial C$ and its inverse. The spatial discretization is then adapted to the present finite volume formulation. WENO reconstructions in finite volume formulations are well-established [31, 32] and are used here for the reconstruction of the interface values.

The main idea of the time discretization is to use a Taylor expansion in time and to replace the resulting time derivatives with spatial derivatives using the governing equation. For the present system, we have $F(C)_t = -uC_x$. Moreover, using the quasilinear form $C_t + uJ(C)^{-1}C_x = 0$, we obtain $F(C)_{tt} = -u(C_t)_x = u^2 \left(J(C)^{-1} C_x \right)_x$.

Using these relations, the second-order Taylor approximation in time, $Q_i^{n+1} \approx Q_i^n + \tau(Q_t)_i^n + \frac{\tau^2}{2}(Q_{tt})_i^n$, leads to

$$Q_i^{n+1} \approx Q_i^n - \tau u C_x \tag{3.6}$$

$$+ \frac{\tau^2 u^2}{2}\left(J(C)^{-1}C_x\right)_x . \tag{3.7}$$

The corresponding second-order explicit scheme is written in the form

$$Q_i^{n+1} = Q_i^n - \tau u D_i^n + \frac{\tau^2 u^2}{2} B_i^n , \tag{3.8}$$

where D_i^n and B_i^n approximate the first and second spatial terms in (3.6) and (3.7), respectively. Their construction is described below using reconstructed values from the previous time level.

For the vector C, we define

$$C_{i+1/2}^n = C_i^n - \frac{1}{2}\left[\omega\left(C_{i-1}^n - C_i^n\right) + (1-\omega)\left(C_i^n - C_{i+1}^n\right)\right] , \tag{3.9}$$

with $\omega \in [0, 1]$. The first spatial derivative in (3.6) is then approximated as

$$D_i^n = \frac{C_{i+1/2}^n - C_{i-1/2}^n}{h} . \tag{3.10}$$

The spatial term $\left(J(C)^{-1}C_x\right)_x$ entering the second-order correction (3.7) is approximated by B_i^n, defined as

$$B_i^n = \frac{A_{i+1/2}^n - A_{i-1/2}^n}{h} , \tag{3.11}$$

where $A_{i+1/2}^n$ and $A_{i-1/2}^n$ approximate $J(C)^{-1}C_x$ at the corresponding locations

$$A_{i+1/2}^n = J(C_{i+1/2}^n)^{-1} D_{i+1/2}^n , \qquad A_{i-1/2}^n = J(C_{i-1/2}^n)^{-1} D_{i-1/2}^n . \tag{3.12}$$

The corresponding approximations of C_x are

$$D_{i+1/2}^n = \frac{C_{i+1/2}^n - C_{i-1/2}^n}{h} , \qquad D_{i-1/2}^n = \frac{C_{i-1/2}^n - C_{i-3/2}^n}{h} . \tag{3.13}$$

The concentration vector C_i^{n+1} is then recovered from $Q_i^{n+1} = F(C_i^{n+1})$ in (3.8), which is solved locally by Newton's method in each finite volume.

Compared with the first-order explicit scheme, the second-order explicit scheme uses a wider stencil because of the reconstruction of interface values and the approximation of spatial derivatives. Therefore, additional neighboring values, or ghost values near the boundary, are required, introduced by extrapolation so that the full stencil can be evaluated. Moreover, despite being explicit with respect to the transport term, the scheme still requires a local Newton iteration due to the nonlinear relation between $F(C)$ and C. In addition, it remains subject to the usual stability restriction on the time step. This makes it unsuitable for the large Courant numbers considered in the numerical experiments below, where the compact implicit schemes can be used with much larger time steps [11, 17, 30].

4. High-resolution schemes

In this section, the term "high-resolution" refers to the ability of the numerical scheme to capture steep gradients and discontinuities while suppressing oscillations, rather than to a higher order of accuracy. This is achieved by combining the second-order scheme with WENO reconstruction and a time limiter.

4.1. High-resolution compact implicit scheme

We now continue with the compact implicit numerical scheme in its high-resolution form. For constant $u > 0$, the high-resolution scheme [14,15] in vector notation adapted to our problem is written using (3.3) as

$$Q_i^{n+1} - Q_i^n + \frac{\tau}{h} u \Big[\Big(C_i^{n+1} - \frac{1}{2} l_i \circ \big(\omega_i \circ (C_{i-1}^{n+1} - C_i^n) + (1-\omega_i) \circ (C_i^{n+1} - C_{i+1}^n)\big) \Big) \\ - \Big(C_{i-1}^{n+1} - \frac{1}{2} l_{i-1} \circ \big(\omega_{i-1} \circ (C_{i-2}^{n+1} - C_{i-1}^n) + (1-\omega_{i-1}) \circ (C_{i-1}^{n+1} - C_i^n)\big) \Big) \Big] = 0\,. \tag{4.1}$$

As mentioned in Section 3.1, $\omega_i = (\omega_{1,i}, \ldots, \omega_{N_c,i})$ and $l_i = (l_{1,i}, \ldots, l_{N_c,i})$ are vectors. The values $\omega_{m,i}$ are obtained from the WENO approximation [16, 26, 27]. A detailed derivation of the WENO approximation for the compact implicit scheme has already been presented in [8,14,15] and is therefore not repeated here, while the values $l_{m,i}$ are computed from the limiter formula [15] for each component m as

$$l_{m,i} = \min\left\{1, \max\left[0, \left(\omega_{m,i} + \frac{1-\omega_{m,i}}{r_{m,i}}\right)^{-1} \left(\frac{2}{\mathrm{Co}_{m,i}} + l_{m,i-1}(\omega_{m,i-1} r_{m,i-1} + 1 - \omega_{m,i-1})\right)\right]\right\}, \quad m = 1, \ldots, N_c\,, \tag{4.2}$$

with

$$r_{m,i} = \frac{c_{m,i-1}^{n+1} - c_{m,i}^n}{c_{m,i}^{n+1} - c_{m,i+1}^n}\,. \tag{4.3}$$

The time limiter is important only for computations with large time steps that are typically controlled. It controls the size of the second-order correction in (4.1). The limiter is constructed using a local Courant number $\mathrm{Co}_{m,i}$, chosen either as $\mathrm{Co}_{\max}$ or $\mathrm{Co}_{i,\max}^{\mathrm{char}}$ (both defined later), which enters the condition used to preserve the non-oscillatory behavior of the high-resolution scheme, see [14,15]. In the present vector case, the choice of this Courant number requires additional attention.

For the scalar Langmuir isotherm (2.6), we have the derivative (2.7), for which the retardation factor is always greater than one. Consequently, the characteristic speed of the scalar equation is given by $u\lambda(c)$, where

$$\lambda(c) = \frac{1}{F'(c)}\,. \tag{4.4}$$

Since $F'(c) > 1$, we have $u\lambda(c) < u$. Therefore, we can define

$$\mathrm{Co}_{\max} = \frac{\tau}{h} u\,, \tag{4.5}$$

which gives an upper bound for the scalar Courant number.

For systems, the role of the retardation factor is played by the Jacobian matrix $J(C) = \partial F(C)/\partial C$. The characteristic speeds are given by the eigenvalues of $J(C)^{-1}$, multiplied by the velocity u.

In all numerical experiments presented here, we assume $u > 0$, so that all characteristic waves propagate from left to right. The corresponding numerical stencils are therefore chosen in the upwind direction. The case of negative transport velocity for scalar equations [14] with Freundlich isotherms, including the corresponding modification of the computational algorithm, was discussed in [8].

Since the eigenvalues of $J(C)$ are positive, and considering the Langmuir sorption, they are larger than or equal to 1. The eigenvalues of $J(C)^{-1}$ are also positive and fall within the range of $(0, 1]$. A large eigenvalue of $J(C)$ corresponds to stronger retardation and hence to a smaller characteristic speed, whereas a small eigenvalue of $J(C)$ corresponds to weaker retardation and faster transport. Therefore, the maximum Courant number can be bounded, as in (4.5), or in terms of the largest eigenvalue of $J(C)^{-1}$. In the numerical experiments below, we first use such an upper bound to choose the time step. Later, for selected test cases, we compute the Courant number more precisely from the eigenvalues of $J(C)^{-1}$, used for the computation of limiter (4.2).

If the upper bound $\mathrm{Co}_{\max}$ (4.5) is used directly in the limiter formula for the system of equations, then the limiting may be too strong for some components. In that case, the values $l_{m,i}$ may be reduced unnecessarily, and the high-resolution scheme is driven too close to the first-order upwind method. This increases numerical diffusion and may reduce the accuracy of the solution, especially in problems where the actual characteristic speeds are significantly smaller than the velocity u because of sorption.

For this reason, in selected computations, we use characteristic Courant numbers based on the eigenvalues of $J(C)^{-1}$. Let $\lambda_{m,i}$, $m = 1, \ldots, N_c$, denote the eigenvalues of $J(C_i)^{-1}$ in the finite volume I_i. The corresponding characteristic Courant numbers are defined by

$$\mathrm{Co}_{m,i}^{\mathrm{char}} = \frac{\tau u}{h} \left|\lambda_{m,i}\right| , \qquad m = 1, \ldots, N_c . \tag{4.6}$$

The maximum characteristic Courant number associated with the finite volume I_i is then

$$\mathrm{Co}_{i,\max}^{\mathrm{char}} = \max_{m=1,\ldots,N_c} \mathrm{Co}_{m,i}^{\mathrm{char}} = \frac{\tau u}{h} \rho\left(J(C_i)^{-1}\right) , \tag{4.7}$$

where ρ denotes the spectral radius. The Courant number used in the limiter (4.2) can therefore be chosen as the local value $\mathrm{Co}_{i,\max}^{\mathrm{char}}$ instead of the global upper bound $\mathrm{Co}_{\max}$ defined in (4.5).

The distinction between the global Courant number bound (4.5) and the local characteristic Courant numbers (4.6) is important. The global upper bound $\mathrm{Co}_{\max}$ depends only on the transport velocity u and does not account for the retardation caused by sorption. In contrast, the local characteristic Courant numbers (4.6) depend on the eigenvalues of $J(C_i)^{-1}$ and therefore reflect the actual characteristic speeds of the system. For the considered Langmuir models, these characteristic Courant numbers do not exceed $\mathrm{Co}_{\max}$ and may be significantly smaller when sorption is strong. Consequently, using characteristic Courant numbers in the time limiter can reduce excessive limiting and numerical diffusion, while preserving the non-oscillatory behavior of the scheme.

In the numerical experiments below, we use $\mathrm{Co}_{\max}$ as a global measure for choosing the time-step size. For the evaluation of the time limiter, we consider two alternatives: the global upper bound $\mathrm{Co}_{\max}$ or the local maximum characteristic Courant number $\mathrm{Co}_{i,\max}^{\mathrm{char}}$ defined in (4.7). The latter choice accounts for the local retardation effects and allows the high-resolution scheme to retain more of its second-order accuracy by avoiding unnecessary limiting.

4.2. WENO approximation in the explicit scheme

For the explicit scheme, parameter ω in (3.9) may change according to the finite volume and is replaced componentwise by $\omega_{m,i}$ for each concentration m and finite volume I_i, and is computed from values at previous time levels. Then $\omega_{m,i}$ can either be fixed or determined adaptively using a WENO procedure. Following again the standard WENO approach [16, 26, 27], also used in [8, 14], we define the upwind and downwind differences for each component by

$$\Delta^{\mathrm{u},n}_{m,i} = c^n_{m,i} - c^n_{m,i-1}\,, \qquad \Delta^{\mathrm{d},n}_{m,i} = c^n_{m,i+1} - c^n_{m,i}\,. \tag{4.8}$$

The corresponding nonlinear weights are

$$a^{\mathrm{u},n}_{m,i} = \frac{\bar{\omega}}{\left(\epsilon_w + \left(\Delta^{\mathrm{u},n}_{m,i}\right)^2\right)^2}\,, \qquad a^{\mathrm{d},n}_{m,i} = \frac{1-\bar{\omega}}{\left(\epsilon_w + \left(\Delta^{\mathrm{d},n}_{m,i}\right)^2\right)^2}\,, \tag{4.9}$$

where $\epsilon_w > 0$ is a small parameter to avoid division by zero and $\bar{\omega}$ is the preferred value. In the computation, we use $\epsilon_w = 10^{-10}$ and $\bar{\omega} = \frac{1}{2}$. The WENO reconstruction parameter is then obtained by

$$\omega_{m,i} = \frac{a^{\mathrm{u},n}_{m,i}}{a^{\mathrm{u},n}_{m,i} + a^{\mathrm{d},n}_{m,i}}\,, \qquad m = 1, \ldots, N_c\,. \tag{4.10}$$

In smooth regions with comparable differences, $\omega_{m,i}$ remains close to $\bar{\omega} = 1/2$.

No additional time limiting is applied in the explicit scheme, and since the explicit time discretization is subject to a stability restriction on the Courant number, sufficiently small time steps have to be used, and the time limiter introduced for the compact implicit scheme to control the second-order correction at large Courant numbers is therefore not required.

5. Numerical experiments

In this section, most of the experiments concern multicomponent models used in chromatography [4, 5, 10]. We present numerical experiments for models with the Langmuir isotherm (2.5). Different choices of the parameters a_m, b_m ($a_m, b_m > 0$) for $m = 1, \ldots, N_c$ are considered in order to test the accuracy and efficiency of the proposed numerical schemes.

In addition, a linear hyperbolic benchmark with a known characteristic decomposition is included [11].

To evaluate the accuracy of the methods, we compute the discrete L^1-error (E) at the final time T. For systems, the error is computed component-wise and summed over all components as

$$E = h \sum_{i=1}^{M} \left(\left| c^N_{1,i} - \bar{c}^N_{1,i} \right| + \ldots + \left| c^N_{N_c,i} - \bar{c}^N_{N_c,i} \right| \right)\,, \tag{5.1}$$

where $\bar{c}^N_{m,i}$ denotes the exact or reference concentration of the m-th component in the i-th finite volume at the final time. The experimental order of convergence (EOC) is then calculated from two consecutive mesh refinements for the examples with the known exact solution or reference solution.

For each of the experiments using Langmuir sorption, we state the upper bound of the Courant number $\mathrm{Co}_{\max}$, based on (4.5). This value is used as a convenient global measure of the time-step size and gives a safe upper bound based only on the transport velocity u. When the high-resolution scheme is used and the limiter is active, we also compute the local characteristic Courant numbers, as described in Section 4.1. These values do not exceed the global upper bound $\mathrm{Co}_{\max}$ in the Langmuir cases considered here, and they are often smaller. For the linear benchmark, the characteristic Courant numbers are considered separately.

The numerical methods were implemented in the Python programming language [33], using the NumPy library [34] for numerical linear algebra and array operations, and the graphical outputs were produced using Matplotlib [35].

5.1. First experiment: Smooth three-component Gaussian profiles

In this experiment, inspired by the test problem considered in [10, 13], we study a smooth three-component problem. The aim is to verify experimentally that the proposed second-order schemes achieve the expected order of accuracy and to compare their computational efficiency.

We prescribe smooth initial data in the form of three Gaussian profiles,

$$c_m^0(x) = \varrho_m \exp(-100(x - 1/2)^2), \quad m = 1, 2, 3, \tag{5.2}$$

with $\varrho_1 = 1$, $\varrho_2 = 2$, $\varrho_3 = 3$. The parameters in Langmuir isotherm [10, 13] are set to $a_1 = 4$, $a_2 = 5$, $a_3 = 6$, $b_1 = b_2 = b_3 = 1$, the velocity $u = 0.2$, and the porosity parameter $\varepsilon = 0.5$, and we compute the numerical solutions on a sequence of refined meshes. For the convergence study, we consider four successively refined meshes with $M = 640$, 1280, 2560, and 5120 finite volumes, corresponding to $N = 128$, 256, 512, and 1024 time steps, respectively.

The reference solution was computed on a fine mesh with $M_{\mathrm{ref}} = 20,480$ up to the final time $T = 0.5$, for $x \in [0, 1]$. For this purpose, we used the implicit second-order scheme with a constant parameter ω. This reference solution was then used for the computation of the discrete errors and the corresponding experimental orders of convergence. Figure 1 shows the comparison between the initial condition and reference solution, for both c_1, c_2, c_3 (right figure) and F_1, F_2, F_3 (left figure).

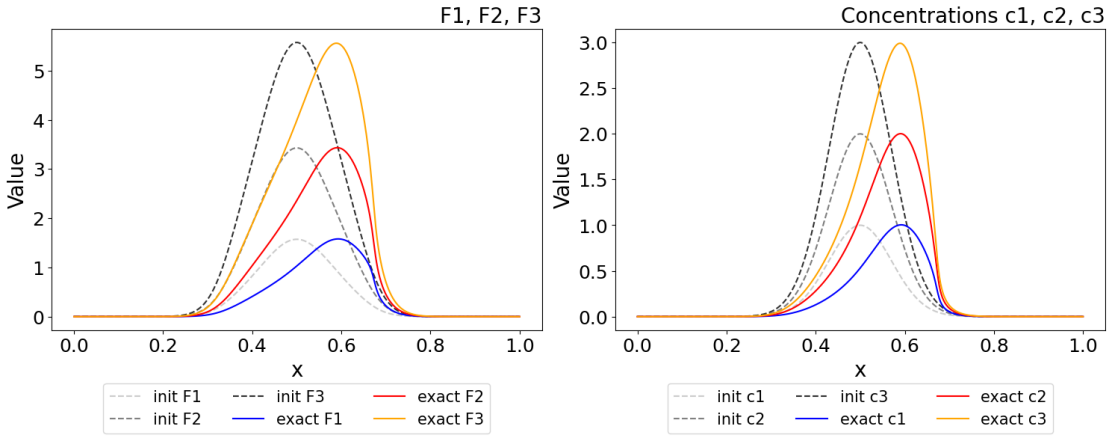


Figure 1. Initial profiles at $t = 0$, see Eq (5.2), and the corresponding reference solution at $T = 0.5$ for the smooth three-component Langmuir problem (Experiment 5.1). The left figure shows the accumulated concentrations F_1, F_2, and F_3, while the right panel shows the mobile concentrations c_1, c_2, and c_3. The reference solution was computed using the second-order compact implicit scheme with the constant reconstruction parameter $\omega = 1/2$ and $M_{\text{ref}} = 20,480$.

The error is measured in the discrete L^1-norm (5.1) and is used to compute the experimental order of convergence. We compare first-order implicit and explicit schemes with second-order schemes. For the second-order discretization, two variants are considered: one with a constant value of the parameter ω set to $1/2$, and one using the WENO approximation. Both implicit and explicit time discretizations are tested.

Since the three components propagate with different characteristic speeds, the corresponding Courant numbers are different, but are smaller than the upper bound Co_{max}. In the comparison involving explicit schemes, the stability restriction is imposed by the explicit WENO discretization. For this reason, we use $\text{Co}_{\text{max}} = 0.5$, which is the largest acceptable value in our computations. Moreover, for such a small Courant number, the additional time limiting of the high-resolution schemes is not engaged and is not needed in this test.

The results reported in Table 1 show decreasing errors under mesh refinement and confirm the expected convergence rates. For both second-order variants, one with the constant reconstruction parameter $\omega = 1/2$ and the other with WENO reconstruction, the errors are of comparable magnitude, with the explicit schemes giving slightly smaller errors on the finer meshes than the implicit scheme.

Table 1. A comparison of the numerical errors E, experimental orders of convergence (EOC), and mean CPU times in seconds for the explicit and implicit first-order schemes, the second-order schemes with the constant reconstruction parameter $\omega = 1/2$, and the second-order schemes with WENO reconstruction in Experiment 5.1. The results are reported for the smooth three-component Gaussian initial data with $\mathrm{Co}_{\max} = 0.5$, where M denotes the number of finite volumes and N the number of time steps. The CPU times are arithmetic means obtained from five runs.

		First order					
		Explicit			Implicit		
M	N	E	EOC	CPU time	E	EOC	CPU time
640	128	$6.8 \cdot 10^{-3}$	-	6.06	$1.5 \cdot 10^{-2}$	-	7.84
1280	256	$3.4 \cdot 10^{-3}$	0.98	21.47	$7.9 \cdot 10^{-3}$	0.97	29.55
2560	512	$1.7 \cdot 10^{-3}$	0.99	58.19	$3.9 \cdot 10^{-3}$	0.98	88.88
5120	1024	$8.7 \cdot 10^{-4}$	0.99	216.29	$2.0 \cdot 10^{-3}$	0.99	342.97
		Second order with constant $\omega = 1/2$					
		Explicit			Implicit		
M	N	E	EOC	CPU time	E	EOC	CPU time
640	128	$2.9 \cdot 10^{-5}$	-	10.23	$7.2 \cdot 10^{-5}$	-	13.78
1280	256	$7.1 \cdot 10^{-6}$	2.04	38.22	$1.8 \cdot 10^{-5}$	2.01	53.33
2560	512	$1.7 \cdot 10^{-6}$	2.02	117.26	$4.4 \cdot 10^{-6}$	2.01	164.74
5120	1024	$3.9 \cdot 10^{-7}$	2.13	449.51	$1.0 \cdot 10^{-6}$	2.05	653.61
		Second order with WENO					
		Explicit			Implicit		
M	N	E	EOC	CPU time	E	EOC	CPU time
640	128	$2.3 \cdot 10^{-4}$	-	10.79	$3.8 \cdot 10^{-4}$	-	20.13
1280	256	$5.2 \cdot 10^{-5}$	2.13	41.50	$9.5 \cdot 10^{-5}$	1.99	81.83
2560	512	$1.1 \cdot 10^{-5}$	2.19	129.12	$2.6 \cdot 10^{-5}$	1.85	258.94
5120	1024	$2.2 \cdot 10^{-6}$	2.38	496.07	$7.0 \cdot 10^{-6}$	1.91	1030.26

The CPU times provide an additional comparison of the methods. As expected, implicit schemes are more computationally expensive, especially when combined with the WENO reconstruction. The additional computational cost of the implicit formulation is considerably more pronounced for the WENO variant than for the second-order scheme with the constant $\omega = 1/2$. Figure 2 presents a work-precision comparison, where the error is plotted as a function of CPU time on a log-log scale. The figure compares first-order schemes, second-order schemes with WENO reconstruction, and second-order schemes with the constant $\omega = 1/2$, for both implicit and explicit time discretizations. The work-precision comparison shows that the relative efficiency depends on the reconstruction. For the small Courant number considered in this experiment, the explicit schemes achieve smaller numerical errors and lower CPU times than their implicit counterparts. The additional computational cost is particularly noticeable for the implicit WENO variant.

The reported CPU times in Table 1 (visualized in Figure 2) were obtained by repeating each

simulation five times and taking the arithmetic mean of the measured values. This averaging was used to reduce the influence of random fluctuations in the computational environment.

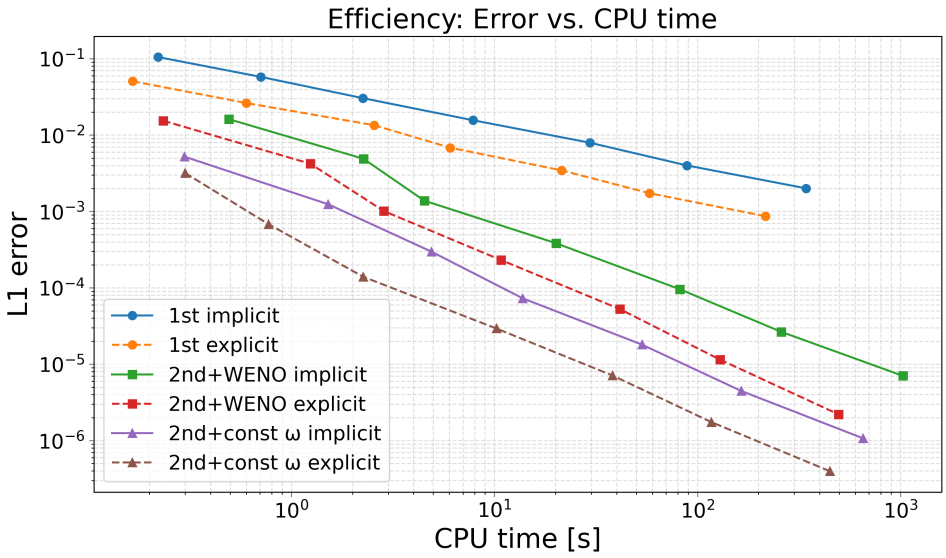


Figure 2. Efficiency comparison of the numerical schemes for Experiment 5.1 in terms of the L^1-error as a function of CPU time. The results are shown on a log-log scale for the explicit and implicit first-order schemes, the second-order schemes with WENO reconstruction, and the second-order schemes with the constant reconstruction parameter $\omega = 1/2$. The computations were performed with $\mathrm{Co}_{\max} = 0.5$, and the CPU times represent arithmetic means over five runs.

Table 2. A comparison of the numerical errors E and experimental orders of convergence (EOC) for the implicit first-order scheme, the compact implicit second-order scheme with the constant reconstruction parameter $\omega = 1/2$, and the compact implicit high-resolution scheme with WENO reconstruction in Experiment 5.1. The results are reported for the smooth three-component Gaussian initial data with $\mathrm{Co}_{\max} = 8$.

		First order		Second order, $\omega = 1/2$		HR with WENO	
M	N	E	EOC	E	EOC	E	EOC
160	2	$3.0 \cdot 10^{-1}$	-	$5.3 \cdot 10^{-2}$	-	$5.3 \cdot 10^{-2}$	-
320	4	$1.3 \cdot 10^{-1}$	0.68	$1.6 \cdot 10^{-2}$	1.70	$1.8 \cdot 10^{-2}$	1.52
640	8	$7.5 \cdot 10^{-2}$	0.79	$4.4 \cdot 10^{-3}$	1.87	$5.7 \cdot 10^{-3}$	1.68
1280	16	$4.0 \cdot 10^{-2}$	0.88	$1.1 \cdot 10^{-3}$	1.94	$1.6 \cdot 10^{-3}$	1.83

Although the explicit schemes are computationally competitive for the small Courant number considered in this experiment, their time step remains restricted by the stability condition. We therefore focus in the following computations on the implicit discretizations and repeat the convergence study with the larger Courant number $\mathrm{Co}_{\max} = 8$ in order to exploit the weaker time-step restriction of the

implicit approach. The corresponding errors and experimental orders of convergence are shown in Table 2. In contrast to the computations with $\mathrm{Co}_{\max} = 0.5$, for the high-resolution WENO variant, the time limiter is active in this test in order to control the second-order correction and suppress spurious oscillations for the larger time steps. The presented results confirm that the implicit schemes can provide stable numerical solutions even for large Courant numbers and preserve, for sufficiently fine grids, the expected EOCs.

5.2. Second experiment: Linear benchmark problem

As the next numerical experiment, we consider a linear system obtained by choosing the accumulation functions in the form

$$\begin{aligned} F_1(c_1, c_2) &= 0.505c_1 - 0.495c_2\,, \\ F_2(c_1, c_2) &= 0.505c_2 - 0.495c_1\,. \end{aligned} \tag{5.3}$$

The corresponding Jacobian matrix is constant,

$$J = \begin{bmatrix} 0.505 & -0.495 \\ -0.495 & 0.505 \end{bmatrix}. \tag{5.4}$$

The eigenvalues of J are 1 and 0.01. Therefore, for $u = 1$, the system contains two characteristic waves propagating with speeds 1 and 100, respectively. The associated eigenvectors are $(1, -1)^T$ and $(1, 1)^T$, hence, the solution can be written as a combination of two traveling waves associated with the slow and fast characteristic variable [11].

This example is useful as a benchmark because it has an explicit analytical structure while still exhibiting two characteristic components with significantly different propagation speeds. It therefore provides a suitable test for verifying the implementation, evaluating experimental convergence rates, and checking whether the numerical method correctly captures both slow and/or fast waves.

We consider two variants of the linear benchmark problem. The first one uses a smooth initial condition, while the second one contains a discontinuity. This allows us to distinguish between the behavior of the schemes in smooth regions, where no limiting is expected to be necessary, and near discontinuities, where limiting plays an essential role.

For the smooth case, we prescribe a Gaussian profile associated only with the slow characteristic component, while the fast characteristic component is set to zero. The exact solution is therefore obtained by shifting the initial profile with the unit speed:

$$c_1(x, t) = \frac{1}{2}\exp\left(-50(x - 1 - t)^2\right), \qquad c_2(x, t) = -\frac{1}{2}\exp\left(-50(x - 1 - t)^2\right). \tag{5.5}$$

Unlike the Langmuir sorption models considered in the other experiments, this linear benchmark allows signed concentration variables and is used solely to investigate the numerical properties of the schemes. Since the solution is smooth, no space or time limiting is applied in this test. We compare the computational efficiency of the first-order scheme and the second-order scheme with the constant $\omega = 1/2$, comparing error E as a function of CPU time.

The computations are performed for a sequence of increasing Courant numbers. Since the linear system contains two characteristic speeds, two Courant numbers are present in each computation. We denote them by Co_S and Co_L, where $\mathrm{Co}_L = 100\,\mathrm{Co}_S$.

The values used in these two experiments are $\mathrm{Co}_L = 12.5, 25, 50, 100, 200, 400, 800$, as reported in Table 3. These large Courant numbers (Co_L) are admissible for the implicit schemes but not for the explicit schemes, which are subject to a much stronger stability restriction.

This restriction is illustrated in Figure 3, where explicit second-order schemes are compared at approximately $t = 0.15$. In the first row, corresponding to $\mathrm{Co}_L = 0.5$, both the constant $\omega = 1/2$ scheme and the scheme with WENO approximation remain stable and non-oscillatory. In the second row, for $\mathrm{Co}_L = 1$, oscillations already appear in the WENO approximation, while the second-order scheme with the constant $\omega = 1/2$ still remains stable. In the third row, corresponding to $\mathrm{Co}_L = 1.25$, both explicit second-order schemes become unstable. This confirms that explicit schemes are not suitable for the large Courant numbers considered in the efficiency comparison.

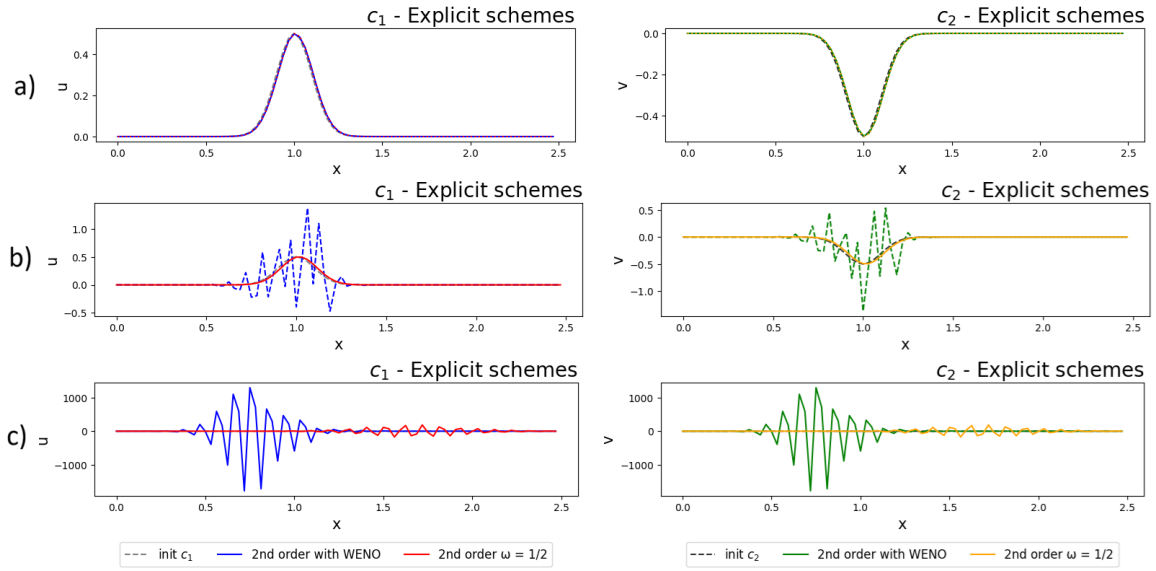


Figure 3. Comparison of two explicit second-order schemes, one using the constant reconstruction parameter $\omega = 1/2$ and the other using WENO reconstruction, for the smooth case of the linear benchmark problem in Experiment 5.2, with the exact Gaussian solution given by (5.5). The results at $t \approx 0.15$ are shown for c_1 in the left column and for c_2 in the right column. From top to bottom, the rows correspond to $\mathrm{Co}_L = 0.5$, 1, and 1.25, denoted by *a*), *b*), and *c*), respectively. Both schemes remain stable for $\mathrm{Co}_L = 0.5$, oscillations appear in the WENO solution for $\mathrm{Co}_L = 1$, and both explicit schemes become unstable for $\mathrm{Co}_L = 1.25$.

Therefore, the following efficiency comparison is restricted to the implicit first-order scheme and the compact implicit second-order scheme with the constant reconstruction parameter $\omega = 1/2$. The corresponding numerical errors E and CPU times for increasing Courant numbers are reported in Table 3.

For this experiment, the choice $\mathrm{Co}_L = 100$, corresponding to $\mathrm{Co}_S = 1$, gives the best overall performance when the second-order scheme with the constant $\omega = 1/2$ is used. This choice leads to the smallest errors among the tested Courant numbers, while still requiring a reasonable CPU time, see Table 3 and Figure 4. This observation is consistent with [14, 15], where different values of ω were tested and the choice $\omega = 1/2$ was shown to give the smallest errors overall. Therefore, $\mathrm{Co}_L = 100$

provides the most favorable balance between accuracy and computational efficiency for this smooth test case. This is an empirical observation rather than a general optimality result. In this experiment, only the slow characteristic wave is present in the solution, while the fast wave is not excited. Therefore, the relevant Courant number for the active wave is $\mathrm{Co}_S = 1$.

Table 3. A comparison of the numerical errors E and CPU times for the implicit first-order scheme and the compact implicit second-order scheme with the constant reconstruction parameter $\omega = 1/2$ for the smooth case of the linear benchmark problem in Experiment 5.2, with the exact Gaussian solution given by (5.5). The computations were performed using $M = 640$ finite volumes for increasing Courant numbers satisfying $\mathrm{Co}_L = 100\,\mathrm{Co}_S$.

		First order implicit		Second order compact implicit with $\omega = 1/2$	
Co_L	Co_S	E	CPU time [s]	E	CPU time [s]
12.5	0.125	$4.40 \cdot 10^{-2}$	11.16	$9.58 \cdot 10^{-4}$	12.73
25	0.25	$4.80 \cdot 10^{-2}$	6.10	$9.17 \cdot 10^{-4}$	6.51
50	0.50	$5.56 \cdot 10^{-2}$	3.38	$7.58 \cdot 10^{-4}$	3.80
100	1.00	$6.93 \cdot 10^{-2}$	1.29	$4.12 \cdot 10^{-4}$	1.51
200	2.00	$9.25 \cdot 10^{-2}$	0.60	$2.94 \cdot 10^{-3}$	0.74
400	4.00	$1.27 \cdot 10^{-1}$	0.32	$1.38 \cdot 10^{-2}$	0.38
800	8.00	$1.73 \cdot 10^{-1}$	0.16	$5.12 \cdot 10^{-2}$	0.27

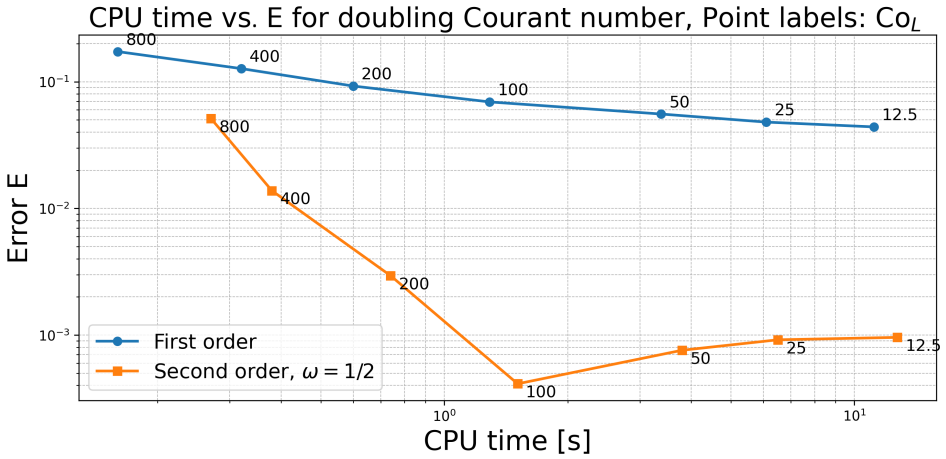


Figure 4. Efficiency comparison of the implicit schemes for the smooth case of the linear benchmark problem in Experiment 5.2, with the exact Gaussian solution given by (5.5). The numerical error E is plotted as a function of CPU time for the implicit first-order scheme and the compact implicit second-order scheme with the constant reconstruction parameter $\omega = 1/2$. The plotted points correspond to the larger Courant numbers Co_L reported in Table 3, with $\mathrm{Co}_L = 100\,\mathrm{Co}_S$ and $M = 640$ finite volumes.

For the discontinuous case, we prescribe a rectangular pulse associated with the slow characteristic

component, again setting the fast component to zero. Since the slow wave propagates with unit speed, the exact solution is

$$c_1(x,t) = \begin{cases} 0.5, & \text{if } 1+t \le x \le 2+t; \\ 0, & \text{otherwise.} \end{cases} \qquad c_2(x,t) = \begin{cases} -0.5, & \text{if } 1+t \le x \le 2+t; \\ 0, & \text{otherwise.} \end{cases} \tag{5.6}$$

In contrast to the Gaussian case, this problem requires limiting in order to control oscillations near the discontinuities. We therefore compare several second-order implicit variants for increasing Courant numbers (see Table 4).

Table 4. A comparison of the numerical errors E and CPU times for the compact implicit second-order scheme with WENO reconstruction without time limiting, the compact implicit high-resolution scheme with WENO reconstruction and the time limiter based on Co_L, and the same high-resolution scheme with the time limiter based on Co_S for the discontinuous case of the linear benchmark problem in Experiment 5.2. The computations were performed using $M = 640$ finite volumes for increasing Courant numbers satisfying $\mathrm{Co}_L = 100\,\mathrm{Co}_S$.

		Second order with WENO		HR with WENO limiter with Co_L		HR with WENO limiter with Co_S	
Co_L	Co_S	E	CPU time [s]	E	CPU time [s]	E	CPU time [s]
12.5	0.125	$3.99 \cdot 10^{-2}$	36.62	$5.92 \cdot 10^{-2}$	235.07	$3.94 \cdot 10^{-2}$	245.54
25	0.25	$4.32 \cdot 10^{-2}$	19.05	$7.96 \cdot 10^{-2}$	118.94	$4.02 \cdot 10^{-2}$	115.44
50	0.50	$5.08 \cdot 10^{-2}$	8.03	$1.00 \cdot 10^{-1}$	60.13	$4.18 \cdot 10^{-2}$	56.96
100	1.00	$4.96 \cdot 10^{-2}$	3.54	$1.26 \cdot 10^{-1}$	30.10	$4.51 \cdot 10^{-2}$	32.04
200	2.00	$6.59 \cdot 10^{-2}$	3.32	$1.61 \cdot 10^{-1}$	15.03	$5.16 \cdot 10^{-2}$	15.95
400	4.00	$1.07 \cdot 10^{-1}$	1.00	$2.12 \cdot 10^{-1}$	10.66	$6.95 \cdot 10^{-2}$	8.68
800	8.00	$2.01 \cdot 10^{-1}$	0.56	$2.88 \cdot 10^{-1}$	6.37	$1.16 \cdot 10^{-1}$	3.79

First, we consider the second-order scheme with only space limiting (WENO approximation), while the time limiter is omitted. Although the corresponding errors in Table 4 appear promising, the numerical profiles in Figure 5 shows visible oscillations for very large Courant numbers, for example, $\mathrm{Co}_L = 800$ and $\mathrm{Co}_S = 8$. Thus, space limiting alone is not sufficient in this regime.

Second, we apply the full high-resolution scheme WENO approximation, combining both space and time limiting. When the time limiter is based on the maximal Courant number Co_L, the method becomes more restrictive and the solution is locally driven closer to first-order accuracy. This leads to larger errors, but improves the non-oscillatory behavior of the numerical solution, see Figure 5.

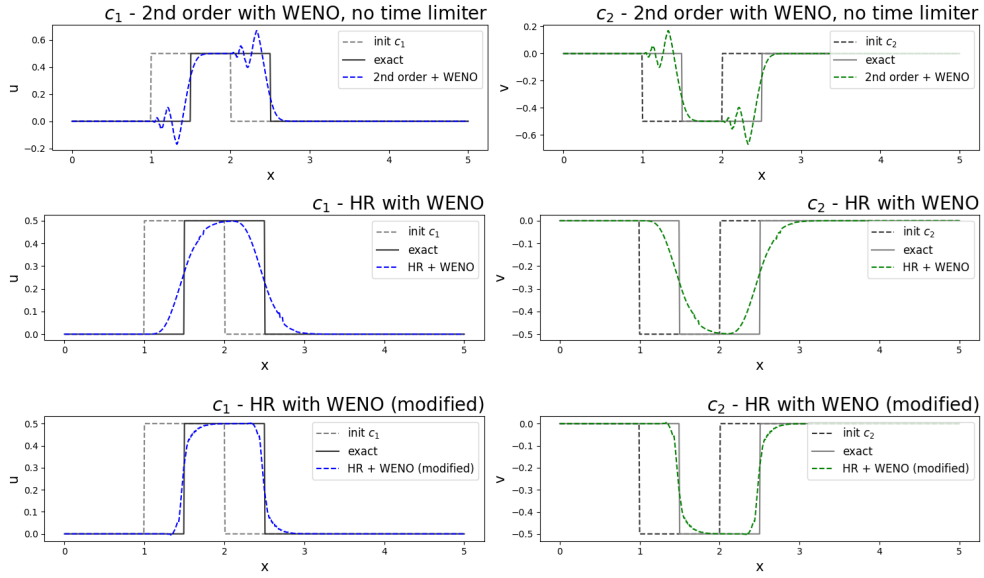


Figure 5. Comparison of the numerical concentration profiles for the discontinuous case of the linear benchmark problem in Experiment 5.2, with $\mathrm{Co}_L = 800$ and $\mathrm{Co}_S = 8$. The results are shown for the compact implicit second-order scheme with WENO reconstruction without time limiting (first row), the compact implicit high-resolution scheme with the time limiter based on Co_L (second row), and the same high-resolution scheme with the time limiter based on Co_S (third row). The WENO scheme without time limiting exhibits visible oscillations near the discontinuities, whereas both high-resolution variants control these oscillations. Using Co_S in the limiter results in sharper and less-diffusive concentration profiles than using Co_L.

Finally, we test a modified time-limiting strategy, where the limiter is based only on the relevant smaller Courant number Co_S associated with the slow characteristic component present in the solution. Since the fast component is absent in this experiment, this choice reduces unnecessary limiting. As a result, the method produces smaller errors (see Figure 6) and gives more accurate profiles than the limiter based on Co_L, while still controlling the oscillations near the discontinuities (see Figure 5).

Since the exact solution contains discontinuities, small numerical oscillations may appear near the wave fronts [25, 27, 36], particularly when higher-order reconstructions are used. Such behavior is a typical feature of high-resolution schemes applied to nonsmooth data [11, 16, 26]. In the present computations, however, these oscillations are not unstable oscillations in the sense of a growing numerical instability. They remain bounded, localized near the discontinuities, and do not destroy the solution. The purpose of the WENO reconstruction is precisely to minimize such spurious oscillations by adapting the reconstruction stencil in nonsmooth regions.

If a strictly non-oscillatory profile is required, the reconstruction may be made more dissipative by applying a stronger limiter, locally reducing the scheme to first order near discontinuities, or using a characteristic-wise reconstruction.

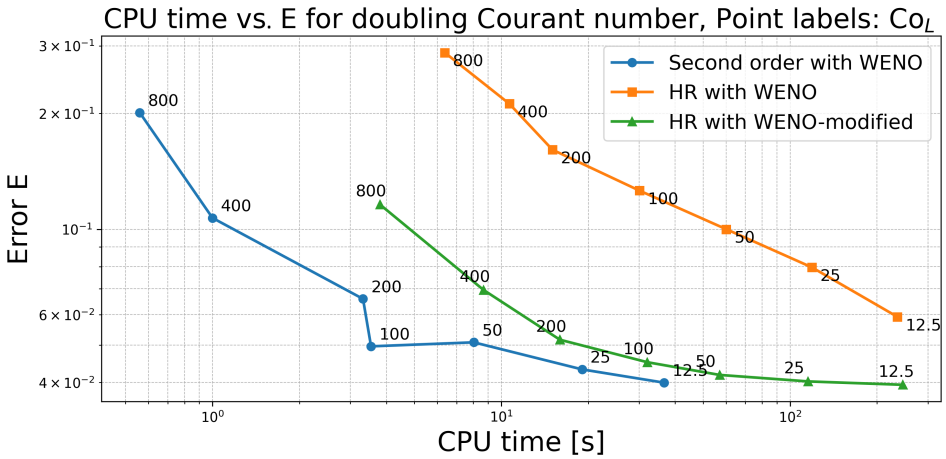


Figure 6. Efficiency comparison of the compact implicit schemes for the discontinuous case of the linear benchmark problem in Experiment 5.2, with the rectangular pulse exact solution. The numerical error E is plotted as a function of CPU time for the second-order scheme with WENO reconstruction without time limiting, the high-resolution scheme with WENO reconstruction and the time limiter based on Co_L, and the high-resolution scheme with WENO reconstruction and the time limiter based on Co_S. The plotted points correspond to the Courant numbers Co_L reported in Table 4, with $\mathrm{Co}_L = 100\,\mathrm{Co}_S$ and $M = 640$ finite volumes.

5.3. Third experiment: Three-component displacement chromatography

In the last numerical experiment, we consider a three-component chromatography problem [13, 20, 21] motivated by the test case proposed in [4, 37] and later used in [10]. The process models the separation of a mixture in a column filled with a solid stationary phase and a liquid moving phase. The mixture contains two solutes, denoted by c_1 and c_2, while the third component, c_3, represents the displacer [4, 21, 37].

The first component is assumed to be less retained than the second one, while the displacer has the strongest affinity to the stationary phase. Therefore, after the displacer is introduced into the column, it progressively replaces the sample components from the stationary phase and pushes them through the column. For sufficiently long columns and suitable adsorption parameters, this process leads to the formation of separated concentration zones [4, 10, 37], usually referred to as a displacement train or an isotachic train [21, 23].

This type of example is commonly used as a benchmark for numerical methods for nonlinear chromatography, since it contains sharp moving transitions and strongly coupled concentration fronts [4, 5, 10]. It tests whether the method can correctly capture the propagation speed of sharp concentration fronts, preserve the separation between components, and reproduce the formation of the displacement train without introducing significant numerical diffusion or spurious oscillations.

Following [4, 10, 23], we use the Langmuir parameters $a_1 = 4$, $a_2 = 5$, $a_3 = 6$ and $b_1 = 4$, $b_2 = 5$, $b_3 = 1$. The porosity parameter is set to $\varepsilon = 0.5$ and velocity $u = 20$.

In contrast to some computations in [4, 10, 13], where generalized Langmuir-type isotherms are also considered, we restrict ourselves to the classical Langmuir isotherm. Hence, the additional

heterogeneity parameter is set to one. Moreover, in the present computations, we neglect axial dispersion ($D = 0$).

Initially, the column contains no transported components, $C(x, 0) = (0, 0, 0)$. The components enter the column through the inlet boundary by means of a prescribed injection profile, and the separation process is generated entirely by the time-dependent inlet data.

The components c_1 and c_2 are injected only during the initial time interval $0 \le t \le 0.1$, both with concentration equal 1. After this injection period, the displacer c_3 is injected continuously with concentration equal to 1 for the first simulation (a) in (5.7)), and $c_3 = 0.5$ for the second simulation (b) in (5.7)). The inlet concentrations are therefore given by

$$a) \quad C_{\text{inj}}(t) = \begin{cases} (1, 1, 0), & 0 \le t \le 0.1, \\ (0, 0, 1), & t > 0.1. \end{cases} \qquad b) \quad C_{\text{inj}}(t) = \begin{cases} (1, 1, 0), & 0 \le t \le 0.1, \\ (0, 0, 0.5), & t > 0.1. \end{cases} \tag{5.7}$$

In the first simulation, the computational domain is chosen for $x \in [0, 100]$ and the mesh contains $M = 1280$ finite volumes. The solution is computed up to the final time $T = 15$. In Figure 7, we show the numerical solution at several times, namely, $t = 1$, $t = 4$, $t = 8$, $t = 11$, and $T = 15$. The computation is performed using the high-resolution scheme with WENO reconstruction and local characteristic Courant numbers in the time limiter.

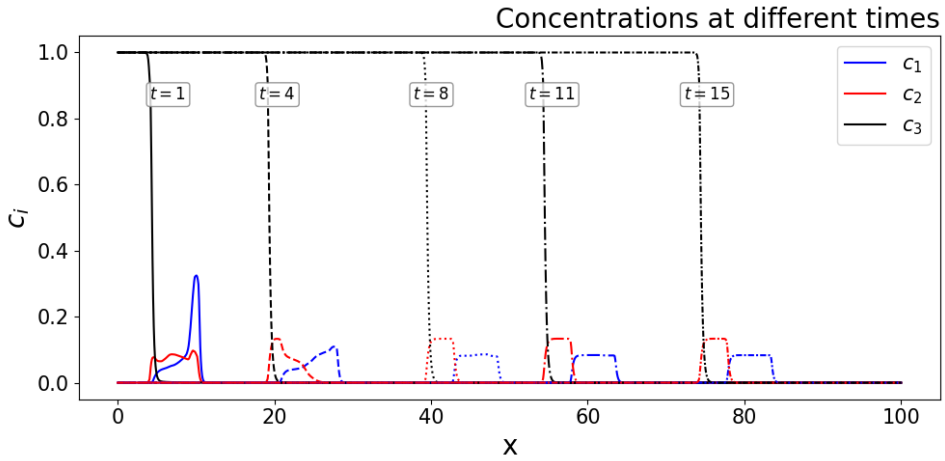


Figure 7. Evolution of the concentration profiles c_1 (blue), c_2 (red), and c_3 (black) for the first inlet profile in (5.7), computed using the high-resolution compact implicit scheme with WENO reconstruction and local characteristic Courant numbers in the time limiter. The solutions are shown at $t \approx 1, 4, 8, 11$ and $T = 15$, with $u = 20$ and $\text{Co}_{\max} = \tau u/h = 12$.

For this simulation, the maximum Courant number obtained from the global bound (4.5) is $\text{Co}_{\max} = 12$. However, this value is not used directly in the time limiter for the results presented in Figure 7, since it may lead to excessive limiting and force the method too strongly toward first-order accuracy. Instead, the relevant local characteristic Courant numbers were computed from the characteristic speeds, see (4.6). In the implementation, this was done using the standard NumPy routines for the inverse matrix and eigenvalue computation.

At the final time step, the maximum values over all finite volumes for the three characteristic fields were approximately 3.43, 4.00, and 4.80. The largest of these values is therefore 4.80. Although this is significantly smaller than the nominal bound $\mathrm{Co}_{\max} = 12$, it is still larger than the stability limit usually required by explicit schemes. This justifies the use of the implicit high-resolution method for this experiment.

To demonstrate the influence of the Courant number used in the time limiter (4.2), we repeated the same simulation using the global bound $\mathrm{Co}_{\max} = 12$ for all concentration components and finite volumes. All other numerical parameters were kept unchanged. The corresponding numerical solutions are presented in Figure 8, allowing a direct comparison with the results obtained using local characteristic Courant numbers in Figure 7.

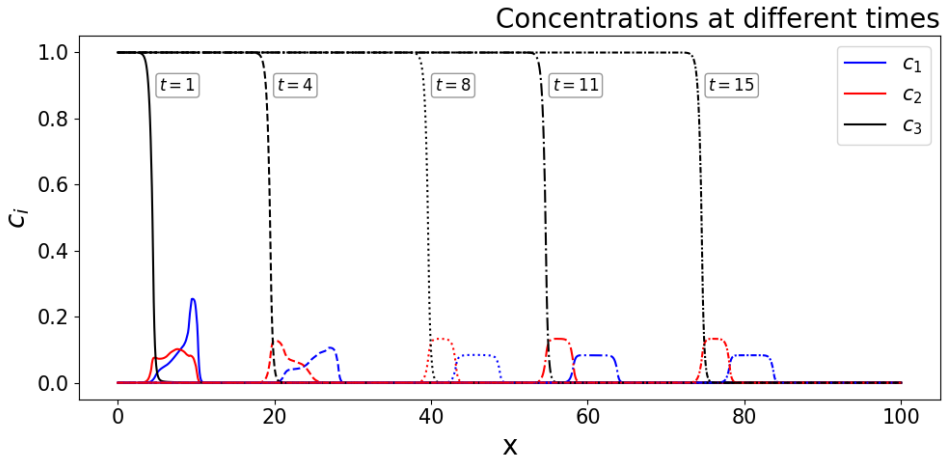


Figure 8. Evolution of the concentration profiles c_1 (blue), c_2 (red), and c_3 (black) for the first inlet profile in (5.7), computed using the high-resolution compact implicit scheme with WENO reconstruction and the global Courant number bound $\mathrm{Co}_{\max} = 12$ in the time limiter (4.2). The solutions are shown at $t \approx 1, 4, 8, 11$ and $T = 15$, with $u = 20$.

Comparing Figures 7 and 8, we observe that using the global Courant number bound $\mathrm{Co}_{\max}$ introduces noticeably more numerical diffusion at all displayed time levels. In contrast, using local characteristic Courant numbers produces sharper concentration profiles, particularly for the concentration c_3, and better preserves the characteristic features of the solution. This difference is especially evident for the concentrations c_1 and c_2 at the first two displayed time levels. In particular, the local maximum of c_1 is better preserved when using characteristic Courant numbers (see $t = 1$), whereas the corresponding peak is significantly reduced when the global bound $\mathrm{Co}_{\max}$ is used. These results demonstrate that accounting for the local characteristic speeds in the time limiter reduces excessive numerical diffusion and improves the resolution of concentration profiles.

The numerical profiles shown in Figure 7 behave as expected for a displacement chromatography process. After the initial injection of components c_1 and c_2, the displacer c_3 enters the column and progressively pushes the sample components forward. As the process develops, the initially overlapping concentrations separate into distinct zones with increasingly sharp interfaces. At the final time, the three components form a well-developed sequence of concentration profiles, indicating an effective displacement and separation process. This behavior is consistent with the corresponding

displacement chromatography experiment reported in [4, 10].

In the second simulation, we use the same computational domain, spatial mesh, final time, and numerical method as in the first simulation. The only difference is the lower concentration of the continuously injected displacer, which is reduced from $c_3 = 1$ to $c_3 = 0.5$ according to the second inlet profile in (5.7). The evolution of the three concentration profiles is shown in Figure 9.

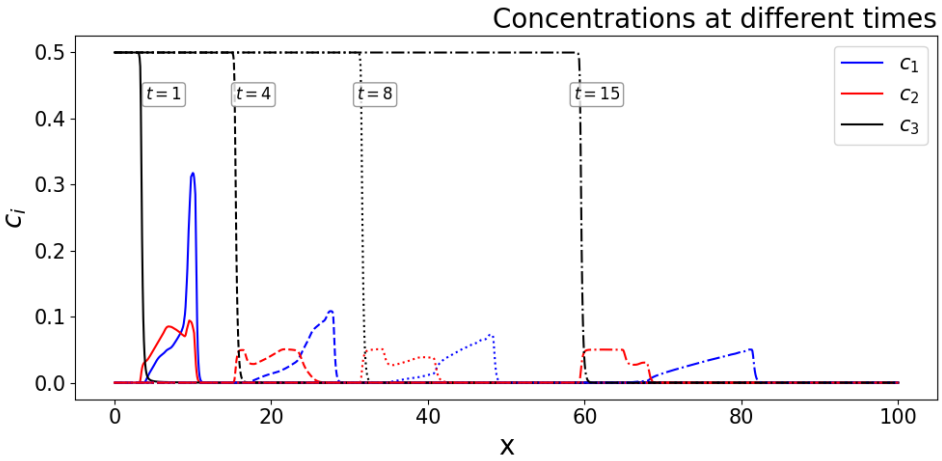


Figure 9. Evolution of the concentration profiles c_1 (blue), c_2 (red), and c_3 (black) for the second inlet profile in (5.7), with the displacer concentration set to $c_3 = 0.5$. The solutions are computed using the high-resolution compact implicit scheme with WENO reconstruction and are shown at $t \approx 1,\ 4,\ 8$ and $T = 15$, with $u = 20$ and $\mathrm{Co}_{\max} = \tau u/h = 12$.

Compared with the first simulation, the lower displacer concentration produces a weaker displacement of the initially injected components. Consequently, the separation of c_1 and c_2 develops more slowly and remains less pronounced at the final time. In particular, the first component does not form the same distinct rectangular concentration zone as in the case where $c_3 = 1$, while the profile of the second component exhibits a less-developed staircase-like structure. Thus, reducing the amount of injected displacer prevents the complete formation of the isotachic train within the considered time interval. This qualitative behavior is consistent with the observations reported in [10] for a reduced displacer concentration.

Overall, the compact implicit high-resolution scheme reproduced the expected displacement behavior with well-resolved concentration fronts and without any visible oscillations, even for the relatively large Courant number $\mathrm{Co}_{\max} = 12$.

6. Conclusions

In this paper, we applied compact implicit high-resolution schemes to multicomponent transport problems with Langmuir sorption. The main difficulty of the system case is the nonlinear coupling introduced by the multicomponent Langmuir isotherm, which leads to a nonlinear retardation matrix and a hyperbolic system with several characteristic speeds.

The numerical experiments show that the proposed compact implicit schemes achieve the expected accuracy for smooth solutions and remain stable for Courant numbers significantly larger than those

admissible for explicit schemes, which still require the nonlinear inversion of the accumulation function and are restricted by a much stronger stability condition.

Special attention was paid to the Courant number used in the limiter. The use of the global bound $\mathrm{Co}_{\max} = \tau u/h$ may lead to excessive limiting, especially when the actual characteristic speeds are reduced by sorption. Therefore, characteristic Courant numbers based on the eigenvalues of $J(C)^{-1}$ were used in selected computations. This strategy reduces unnecessary numerical diffusion and allows the high-resolution scheme to preserve more of its second-order accuracy.

The chromatography examples demonstrate that the method is able to capture sharp moving fronts and the formation of displacement trains in multicomponent Langmuir systems.

Despite these advantages, the proposed method has certain limitations. Although the high-resolution scheme significantly reduces oscillations, small oscillations may still occur near discontinuities. A possible direction for future research is to apply WENO reconstruction in characteristic variables rather than directly to the concentration components, which may further improve the non-oscillatory behavior of the method. Another challenge is the extension of the proposed compact implicit scheme to higher orders of accuracy. A third-order accurate compact implicit scheme has already been investigated for smooth solutions in [38]. However, extending such an approach to nonsmooth solutions while maintaining high-resolution properties is considerably more challenging. Furthermore, preserving the compact structure and computational efficiency of higher-order schemes remains an important direction for future research.

Further research will also focus on extending the proposed approach to more general transport problems. We have already investigated two-dimensional transport with Freundlich sorption on uniform square grids in [8], obtaining promising numerical results. However, extensions to nonuniform grids and more complex geometries remain challenging, particularly because of the selection of appropriate upwind stencils. We also plan to investigate the incorporation of diffusion and dispersion effects. These extensions would allow the method to address more realistic transport processes in porous media and chromatographic systems.

Author contributions

Dagmar Žáková: Conceptualization, Methodology, Software, Formal analysis, Validation, Visualization, Writing–original draft, Writing–review and editing; Peter Frolkovič: Conceptualization, Methodology, Formal analysis, Supervision, Validation, Writing–original draft, Writing–review and editing. All authors have read and approved the final version of the manuscript for publication.

Use of Generative-AI tools declaration

The authors declare they have used ChatGPT (OpenAI) during the preparation of this manuscript for language editing, text revision, and consistency checks. No AI tools were used to generate the source code, numerical results, or figures presented in this work.

Acknowledgments

This work was supported by the Slovak Research and Development Agency (APVV) under grant No. VV-MVP-24-0116 and by the Scientific Grant Agency of the Ministry of Education, Research, Development and Youth of the Slovak Republic and the Slovak Academy of Sciences (VEGA) under grant No. 1/0314/23.

Conflict of interest

The authors declare no conflicts of interest.

References

1. M. L. Brusseau, The effect of nonlinear sorption on transformation of contaminants during transport in porous media, *J. Contam. Hydrol.*, **17** (1995), 277–291. https://doi.org/10.1016/0169-7722(94)00041-F
2. J. Kačur, B. Malengier, M. Remešíková, Solution of contaminant transport with equilibrium and non-equilibrium adsorption, *Comput. Method. Appl. M.*, **194** (2005), 479–489. https://doi.org/10.1016/j.cma.2004.05.017
3. S. B. Patil, H. S. Chore, Contaminant transport through porous media: An overview of experimental and numerical studies, *Ad. Environ. Res.*, **3** (2014), 45–69.
4. S. Javeed, S. Qamar, A. Seidel-Morgenstern, G. Warnecke, Efficient and accurate numerical simulation of nonlinear chromatographic processes, *Comput. Chem. Eng.*, **35** (2011), 2294–2305. https://doi.org/10.1016/j.compchemeng.2010.10.002
5. R. Bürger, P. Mulet, L. Rubio, M. Sepúlveda, Linearly implicit-explicit schemes for the equilibrium dispersive model of chromatography, *Appl. Math. Comput.*, **317** (2018), 172–186. https://doi.org/10.1016/j.amc.2017.09.006
6. K. Meyer, S. Leweke, E. von Lieres, J. K. Huusom, J. Abildskov, ChromaTech: A discontinuous Galerkin spectral element simulator for preparative liquid chromatography, *Comput. Chem. Eng.*, **141** (2020), 107012. https://doi.org/10.1016/j.compchemeng.2020.107012
7. P. Frolkovič, M. Lampe, G. Wittum, Numerical simulation of contaminant transport in groundwater using software tools of r^3t, *Comput. Visual. Sci.*, **18** (2016), 17–29. https://doi.org/10.1007/s00791-016-0268-0
8. D. Žáková, P. Frolkovič, Compact implicit high resolution numerical method for solving transport problems with sorption isotherms, *Tatra Mountains Mathematical Publications*, **91** (2025), 153–178. https://doi.org/10.2478/tmmp-2025-0030
9. M. A. Rasheed, S. Perveen, S. Qamar, Simulation of nonlinear and nonisothermal reactive liquid chromatography considering finite mass-transfer rates and various adsorption scenarios, *ACS Omega*, **9** (2024), 47284–47308. https://doi.org/10.1021/acsomega.4c08414
10. R. Donat, M. C. Martí, P. Mulet, WENO scheme on characteristics for the equilibrium dispersive model of chromatography with generalized Langmuir isotherms, *Appl. Numer. Math.*, **201** (2024), 247–264. https://doi.org/10.1016/j.apnum.2024.03.006

11. R. J. LeVeque, *Finite-volume methods for hyperbolic problems*, Cambridge: Cambridge University Press, 2002. https://doi.org/10.1017/CBO9780511791253
12. P. Frolkovič, J. Kačur, Semi-analytical solutions of a contaminant transport equation with nonlinear sorption in 1D, *Comput. Geosci.*, **10** (2006), 279–290. https://doi.org/10.1007/s10596-006-9023-9
13. R. Donat, F. Guerrero, P. Mulet, Implicit–explicit WENO scheme for the equilibrium dispersive model of chromatography, *Appl. Numer. Math.*, **123** (2018), 22–42. https://doi.org/10.1016/j.apnum.2017.08.008
14. P. Frolkovič, D. Žáková, Numerical solution of two dimensional scalar conservation laws using compact implicit numerical schemes on Cartesian meshes, *ESAIM-Math. Model. Num.*, **60** (2026), 247–272. https://doi.org/10.1051/m2an/2025097
15. P. Frolkovič, M. Žeravỳ, High resolution compact implicit numerical scheme for conservation laws, *Appl. Math. Comput.*, **442** (2023), 127720. https://doi.org/10.1016/j.amc.2022.127720
16. C.-W. Shu, Essentially non-oscillatory and weighted essentially non-oscillatory schemes for hyperbolic conservation laws, In: *Advanced numerical approximation of nonlinear hyperbolic equations*, Berlin: Springer, 1998, 325–432. https://doi.org/10.1007/bfb0096355
17. K. Duraisamy, J. D. Baeder, Implicit scheme for hyperbolic conservation laws using nonoscillatory reconstruction in space and time, *SIAM J. Sci. Comput.*, **29** (2007), 2607–2620. https://doi.org/10.1137/070683271
18. G. Puppo, M. Semplice, G. Visconti, Quinpi: Integrating conservation laws with CWENO implicit methods, *Commun. Appl. Math. Comput.*, **5** (2023), 343–369. https://doi.org/10.1007/s42967-021-00171-0
19. E. Lozano, T. D. Aslam, Implicit fast sweeping method for hyperbolic systems of conservation laws, *J. Comput. Phys.*, **430** (2021), 110039. https://doi.org/10.1016/j.jcp.2020.110039
20. T. Y. Gu, *Mathematical mdeling and scale-up of liquid chromatography: with application examples*, Cham: Springer, 2015. https://doi.org/10.1007/978-3-319-16145-7
21. H. Schmidt-Traub, M. Schulte, A. Seidel-Morgenstern, *Preparative chromatography*, Hoboken: John Wiley & Sons, 2020. https://doi.org/10.1002/9783527816347
22. G. Guiochon, A. Felinger, D. G. Shirazi, *Fundamentals of preparative and nonlinear chromatography*, 2 Eds., Boston: Academic Press, 2006.
23. M. Mazzotti, Nonclassical composition fronts in nonlinear chromatography: delta-shock, *Ind. Eng. Chem. Res.*, **48** (2009), 7733–7752. https://doi.org/10.1021/ie9001537
24. R. Donat, P. Mulet, A secular equation for the Jacobian matrix of certain multispecies kinematic flow models, *Numer. Meth. Part. D. E.*, **26** (2010), 159–175. https://doi.org/10.1002/num.20423
25. A. Harten, High resolution schemes for hyperbolic conservation laws, *J. Comput. Phys.*, **135** (1997), 260–278. https://doi.org/10.1006/jcph.1997.5713
26. C.-W. Shu, S. Osher, Efficient implementation of essentially non-oscillatory shock-capturing schemes, *J. Comput. Phys.*, **77** (1988), 439–471. https://doi.org/10.1016/0021-9991(88)90177-5
27. G.-S. Jiang, C.-W. Shu, Efficient implementation of weighted ENO schemes, *J. Comput. Phys.*, **126** (1996), 202–228. https://doi.org/10.1006/jcph.1996.0130

28. P. K. Sweby, High resolution schemes using flux limiters for hyperbolic conservation laws, *SIAM J. Numer. Anal.*, **21** (1984), 995–1011. https://doi.org/10.1137/0721062

29. H. K. Zhao, A fast sweeping method for Eikonal equations, *Math. Comp.*, **74** (2005), 603–627. https://doi.org/10.1090/S0025-5718-04-01678-3

30. J. X. Qiu, C.-W. Shu, Finite difference WENO schemes with Lax–Wendroff-type time discretizations, *SIAM J. Sci. Comput.*, **24** (2003), 2185–2198. https://doi.org/10.1137/S1064827502412504

31. J. X. Qiu, C.-W. Shu, On the construction, comparison, and local characteristic decomposition for high-order central WENO schemes, *J. Comput. Phys.*, **183** (2002), 187–209. https://doi.org/10.1006/jcph.2002.7191

32. C.-W. Shu, High order weighted essentially nonoscillatory schemes for convection dominated problems, *SIAM Rev.*, **51** (2009), 82–126. https://doi.org/10.1137/070679065

33. G. van Rossum, *Python tutorial*, CWI Report CS-R9526, Centrum voor Wiskunde en Informatica, Amsterdam, 1995.

34. C. R. Harris, K. J. Millman, S. J. van der Walt, R. Gommers, P. Virtanen, D. Cournapeau, et al., Array programming with NumPy, *Nature*, **585** (2020), 357–362. https://doi.org/10.1038/s41586-020-2649-2

35. J. D. Hunter, Matplotlib: A 2D graphics environment, *Comput. Sci. Eng.*, **9** (2007), 90–95. https://doi.org/10.1109/MCSE.2007.55

36. A. Harten, B. Engquist, S. Osher, S. R. Chakravarthy, Uniformly high order accurate essentially non-oscillatory schemes, III, *J. Comput. Phys.*, **131** (1997), 3–47. https://doi.org/10.1006/jcph.1996.5632

37. J. Frenz, High-performance displacement chromatography, In: *High-performance liquid chromatography: advances and perspectives*, New York: Academic Press, 1988, 211–314. https://doi.org/10.1016/b978-0-12-312205-6.50007-2

38. D. Žáková, P. Frolkovič, Higher order compact implicit finite volume schemes for scalar conservation laws, In: *Hyperbolic problems: theory, numerics, applications, Volume II*, Cham: Springer, 2024, 221–231. https://doi.org/10.1007/978-3-031-55264-9_19



AIMS Press

© 2026 the Author(s), licensee AIMS Press. This is an open access article distributed under the terms of the Creative Commons Attribution License (https://creativecommons.org/licenses/by/4.0)